Journal of
Materials Chemistry C

ROYAL SOCIETY
OF CHEMISTRY

PAPER

View Article Online
View Journal

Check for updates

Cite this: DOI: 10.1039/d5tc02874d

Received 30th July 2025,
Accepted 3rd January 2026

DOI: 10.1039/d5tc02874d

rsc.li/materials-c

Synthesis of metal nitride and metal oxide nanoparticles by atmospheric-pressure spark ablation

Klito C. Petallidou, †*[a] Dimitris Gounaris,†[a] Pau Ternero, [b]
Maria E. Messing, [bc] Andreas Schmidt-Ott[ade] and George Biskos *[af]

Metal nitride and metal oxide nanoparticles (NPs) provide key material components for a number of applications due to their unique properties. Here we demonstrate that spark ablation of metallic electrodes, quenched with a pure N_2 flow at atmospheric pressure, can be used as a reactive generator to synthesize metal nitride, metal oxide or pure metallic NPs depending on the material. The composition of the synthesized NPs was determined through their crystal structure using X-ray diffraction and transmission electron microscopy (TEM). Our results show that the composition of the resulting NPs strongly depends on the electrode material: Ti and Al form mixtures of metal nitride and oxide NPs, whereas Mg and Pd produce respectively only oxide and pure metallic NPs. Repeated XRD measurements of the samples after exposing them to ambient air over periods of several months showed that the stability of TiN was higher compared to that of the AlN NPs, with the first being converted to TiN_yO_x and the latter to γ-Al_2O_3 after 9 months.

1. Introduction

Metal nitride nanoparticles (NPs), due to their unique properties, comprise unique building blocks of nanomaterials that can be used in a number of applications.[1] They have strong plasmonic responses, high melting points, chemical resistances and thermal stabilities,[2,3] while they can be produced at a relatively low cost.[4,5] Because of their unique properties, they are considered excellent alternatives to noble metals for a number of catalytic reactions,[1,6–9] in sensing because among others they can attribute high selectivity,[10,11] as well as in energy storage including batteries and supercapacitors.[12,13]

Similarly, metal oxide NPs have extensively been employed as building blocks of materials with highly diverse properties. Their wide chemical versatility and tunable electronic structure can attribute unique optical, catalytic, and semiconducting characteristics, enabling several emerging applications.[14] As a result, they have been employed in catalysis,[15,16] and gas-sensing,[17,18] as well as in energy-storage[19,20] where they attribute efficient charge transfer and long-term cycling performance.[21] Overall, this diversity of applications underline the important role of metal oxide NPs, which is complementary or synergistic to that of their metal nitride counterparts in advanced materials.

Metal nitrides and oxides can be classified based on the type of bonds between their atoms: *i.e.*, metal–metal for both, metal–nitrogen (M–N) for the nitrides, and metal–oxygen (M–O) for the oxides. Nitrides containing groups I and II metals form ionic M–N bonds that exhibit high conductivity (*e.g.*, Li–N in Li_3N).[22] In contrast, nitrides of elements in groups III and IV predominantly form covalent M–N bonds and thus exhibit an ionic character, yielding semi-conductive or non-conductive materials with high hardness and elevated degradation and/or melting points.[23] Transition-metal nitrides, on the other hand, exhibit a combination of ionic and covalent M–N bonds, as well as metallic bonds between metal atoms, and thus display a wide range of physical and chemical properties.[24] Similarly, metal oxides can be classified according to the nature of the M–O bonds and the metal cation involved. Oxides of alkali and alkaline-earth metals typically form highly ionic M–O bonds, yielding wide-bandgap insulating materials with high thermal stability.[25] Transition-metal oxides, on the other hand, display a more complex mixture of ionic, covalent or metallic bonding, depending on the metal oxidation state and the local coordination environment.[26] This bonding diversity leads to a

---

[a] Climate and Atmosphere Research Centre, The Cyprus Institute, 2121 Nicosia, Cyprus. E-mail: k.petallidou@cyi.ac.cy, g.biskos@cyi.ac.cy
[b] Department of Physics and NanoLund, Lund University, 22100 Lund, Sweden
[c] Department of Microtechnology and Nanoscience, Chalmers University of Technology, 412 96 Gothenburg, Sweden
[d] Faculty of Applied Sciences, Delft University of Technology, 2629 HZ Delft, The Netherlands
[e] VSPARTICLE B.V, 2629 JD Delft, The Netherlands
[f] Faculty of Civil Engineering and Geosciences, Delft University of Technology, 2628 CN Delft, The Netherlands. E-mail: g.biskos@tudelft.nl

† These authors contributed equally to this work.

broad spectrum of properties, including conductivity, magnetism, and reactivity, which is the reason they are widely used in catalysis, sensing, and energy-storage applications.[27–29]

Metal nitride and oxide NPs can be synthesized through chemical or physical methods.[1] Chemical methods for producing metal nitride NPs typically involve the reaction of metals with NH_3 or N_2. These methods, however, are energy demanding as they require elevated temperatures (800–2000 °C) and extended synthesis periods, while they carry a risk of contamination from undesired side reactions. Chemical routes for synthesizing metal oxide NPs include sol–gel, co-precipitation, hydrothermal or combustion methods.[30] These approaches provide good control over particle size, morphology and composition. However, they often require careful control of synthesis conditions (*e.g.*, temperature and/or pH) and typically generate byproducts that need to be disposed.[31] Physical methods for producing both metal nitride and oxide NPs, on the other hand, offer attractive alternatives due to their simplicity. The operating pressures of physical methods can range from ultra-high or high vacuum (*e.g.*, physical vapor deposition, PVC), to atmospheric (*e.g.*, laser- and plasma-assisted). Among those operated at atmospheric pressure, plasma-assisted techniques[32–35] are particularly attractive due to their relatively low cost.

Spark ablation, which is a plasma-assisted technique, is a gas-phase/aerosol-based method for synthesizing well-defined NPs,[36] having a number of advantages.[37] It uses spark discharges between two metal electrodes, heating them locally at temperatures that vaporize small amounts of material from their surface. The resulting vapors are quenched by a carrier gas flowing between the two electrodes, thereby nucleating to form atomic clusters that subsequently grow to NPs upon condensation and coagulation. NP production by this method depends on the energy input to the system, the quenching flow rate, the ablatability of the material and the diameter of the electrodes employed.[38] Spark ablation can produce NPs spanning a broad size range, from clusters containing only a few atoms[39] and singlet NPs having diameters of several nanometers,[40] to agglomerated structures that extend from tens to hundreds of nanometers.[41] One of the key benefits of this technique is its ability to precisely control the size[41–43] and composition[44–46] of the resulting NPs in a simple, cost-effective, and environmentally friendly way, as it eliminates the need for chemical precursors and thus does not produce any wastes.

In a previous study, we observed that using N_2 as a carrier gas in atmospheric-pressure spark ablation leads to NP production instabilities that are attributed to the formation of nitrides on the electrode surface.[47] However, the extent to which the resulting NPs undergo nitridation in this process remains unknown. While the ability of spark ablation to form metal oxide NPs is well understood,[48,49] and to a certain extent is hard to avoid due to trace amounts of O_2 that are present on the electrodes and/or in the carrier gases,[50,51] very few recent studies have reported on the ability of the process to form metal nitrides NPs. To this end, Elmroth Nordlander *et al.*[52] have demonstrated that the method can be used to synthesize Janus-type Mo/Mo_3Ni_2N NPs when using respectively pure N_2 or a H_2/N_2 gas mixture as a carrier gas. Radovanović-Perić *et al.*[53] have reported production of titanium nitride NPs, whereas more recently, Signore *et al.*[54] investigated the effect of spark current on the synthesis of mixed copper oxide and copper nitride NPs. These works, however, focus on specific materials and conditions, and understanding of how formation of nitride NPs can compete formation of their oxide counterparts in spark ablation and across different metals and process parameters is still missing.

Here we evaluate the effectiveness of spark ablation for producing a range of metal nitride and oxide NPs, thereby expanding the findings from previous works. To systematically investigate the largely unexplored nitride formation mechanisms and how this competes oxidation, we selected a range of elements, including one from group II (Mg), one from group III (Al), and two transition metals (Pd and Ti). Additionally, we carried out tests to assess the chemical stability of the resulting NPs over time.

2. Experimental

The experimental set-up was the same as the one used in our previous works.[44,47] In brief, we employed a commercial Spark Discharge Generator (SDG; VSParticle Model G1, Fig. S1 in the SI), to synthesize NPs using pure N_2 as a carrier gas (2 L min^{-1}, 99.999% purity), and high-purity electrodes (99.6% for Ti, 99.95% for Al, 99.95% for Pd, and 97% for Mg) having diameters of 2 (for Ti and Pd) or 3 (for Al and Mg) mm. The mean voltage between the two electrodes was set to 1.0 kV, and considering that the capacitance of the systems is fixed to 20 nF, the resulting energy per spark was 22.5 mJ. The experimental setup used to measure the size distributions of the NPs and to deposit them on grids (Lacey carbon type-A, 300 mesh, copper grids, Prod. No. 01890, Ted Pella) for transmission electron microscope (TEM) analysis, as well as on filters for XRD measurements, is described in detail in our previous work.[44]

A scanning mobility particle sizer (SMPS) was used to measure the size distributions of the NPs generated by the SDG. The SMPS included a differential mobility analyzer (DMA; TSI Model 3081) coupled with an ^{241}Am aerosol neutralizer (GRIMM Model 5.522), an electrostatic classifier (TSI Model 3080), and an ultrafine water-based condensation particle counter (CPC; TSI Model 3786). The DMA voltage in the SMPS was scanned from 0.01 to 9.95 kV over 3 minutes, enabling NP size distribution measurements from 7 to 305 nm. The aerosol and sheath flows through the DMA were set to 0.6 and 6.0 L min^{-1}, respectively, in all the measurements.

XRD analysis of NP samples collected in the form of powders was carried out using a MiniFlex 600 benchtop diffractometer (Rigaku; CuKα radiation, λ = 1.5418 Å). The diffraction angle, 2θ, in the diffractometer ranged from 20° to 80°, with a scanning speed of 10° min^{-1}, while the mean crystallite size was estimated using the Scherrer formula.[55]

A High-Resolution TEM (HR-TEM; Jeol JEM-3000F) with scanning/transmission operating modes (STEM) was used to estimate the spacing of adjacent crystal planes as the average of 10 different measurements. The HR-TEM images were analyzed using ImageJ.[56]

3. Results

Fig. 1 shows size distributions, measured with the SMPS, and XRD diffractograms of the NPs produced by the SDG using Ti, Al, Pd, and Mg electrodes with N_2 as the carrier gas. The geometric mean diameters of the NPs are in the order of 43–45 nm when the Ti and Pd electrodes are employed in the SDG, *ca.* 75 nm for the Mg and slightly higher than 100 nm for the Al electrodes, following the same trend with the ablatability of the material:[38] *i.e.*, the higher the ablatability the higher the evaporation rate, and thus the initial concentration of the resulting vapors that consequently defines the size of the resulting particles.

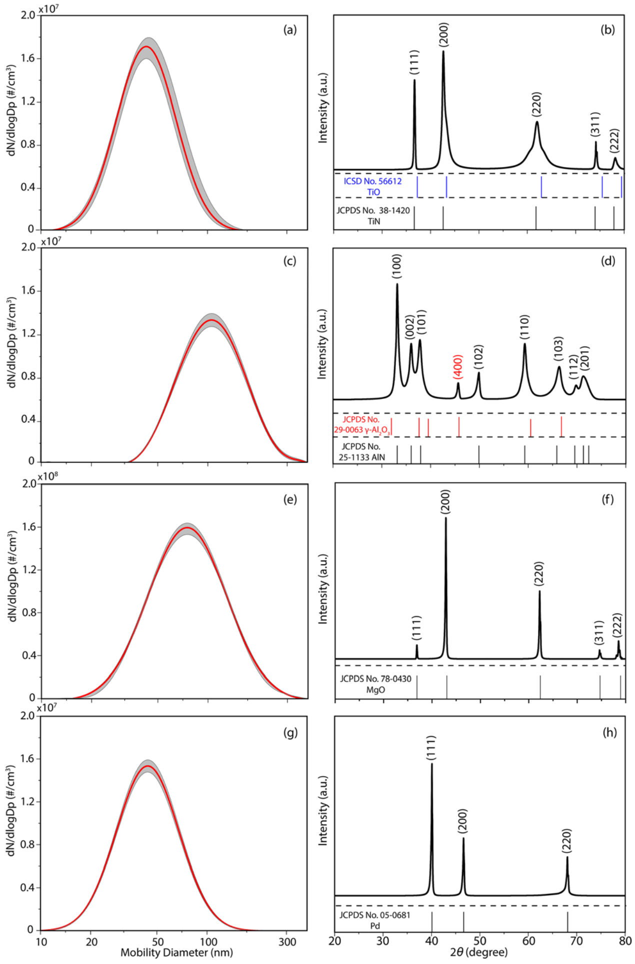

Fig. 1 Particle size distributions of as-deposited NPs measured by the SMPS (left plots), and diffractograms by the XRD system (right plots) when using (a) and (b) Ti, (c) and (d) Al, (e) and (f) Mg, and (g) and (h) Pd electrodes in the SDG, with N_2 as a carrier gas. The numbers in the brackets in the XRD measurements are the Miller indices, whereas the lines below the diffractograms show data from corresponding libraries.

The XRD analysis of the NPs prepared using the Ti electrodes in the SDG (Fig. 1b) exhibit peaks at 36.7°, 42.6°, 62.1°, 74.3°, and 78.2° that correspond to the (111), (200), (220), (311), and (222) crystallographic planes of the cubic structure of TiN (JCPDS# 38-1420). Closer analysis of these results shows that the peaks at 42.6° and 62.1° have shoulders at higher 2θ values, which correspond to TiO (ICSD# 56612). This is not surprising as TiO can form from traces amount of oxygen in the carrier gas or by exposure of the NPs to ambient air after synthesis. We should note here that the peak at 62.1° appears as a shoulder at lower 2θ value, indicating the presence of TiN_x with $x < 1$. The titanium nitride NPs reported previously by Radovanović-Perić *et al.*[57] also exhibit broad diffraction peaks, which indicate the presence of additional Ti phases, such as oxides, in agreement with our observations.

The XRD measurements of the NPs prepared using the Al electrodes (Fig. 1d), exhibit peaks at 33.1°, 36.0°, 37.8°, 49.9°, 59.2°, 66.3°, 69.7°, and 71.1° which correspond to (100), (002), (101), (102), (110), (103), (112) and (201) of the hexagonal AlN (JCPDS# 25-1133). The XRD pattern has an additional peak at 45.7° which can be attributed to the (222) crystallographic plane of γ-Al_2O_3. As observed for the Ti electrodes, the diffraction peaks obtained using Al electrodes are broad and partially overlapping, indicating the coexistence of nitride and oxide phases. The formation of γ-Al_2O_3 under N_2 is therefore attributed to trace amounts of oxygen in the gas stream and/or exposure to ambient air after the experiment, similar to the behavior observed for the Ti-based NPs.

Fig. 1f shows the XRD analysis corresponding to the NPs produced using Mg electrodes in the SDG. The diffractogram shows peaks at 36.8°, 42.9°, 62.2°, 74.7°, and 78.6°, which correspond to the (111), (200), (220), (311), and (222) crystallographic planes of the periclase structure of MgO (JCPDS# 78-0430). Magnesium readily forms oxides because of its very strong affinity for oxygen, driven by its highly electropositive character and the large thermodynamic stability of MgO.[58]

The diffractogram of as-deposited NPs produced using Pd electrodes in the SDG (Fig. 1h) exhibits peaks at 40.1°, 46.6°, and 68.1°, which correspond to the (111), (200), and (220) crystallographic planes of cubic Pd (JCPDS# 05-0681). As a noble metal, having high electronegativity, a filled d-band and low affinity for both oxygen and nitrogen, Pd does not form stable nitrides or oxides. As a result, bulk PdO is only metastable and decomposes upon mild heating, while palladium nitrides are thermodynamically unstable and cannot be synthesized under conventional conditions.

Similar results for NPs produced by spark ablating Hf, V, and Mn electrodes are provided in the SI (see Fig. S2).

The crystallite sizes of all identified phases were estimated using the Scherrer equation.[59] The crystallite size of TiN was determined from a diffraction peak at 36.7°, which does not overlap with other reflections, and was found to be 37.8 nm. The crystallite size of the hexagonal AlN phase was estimated from the peak at 49.9° and found to be 14.4 nm, while that

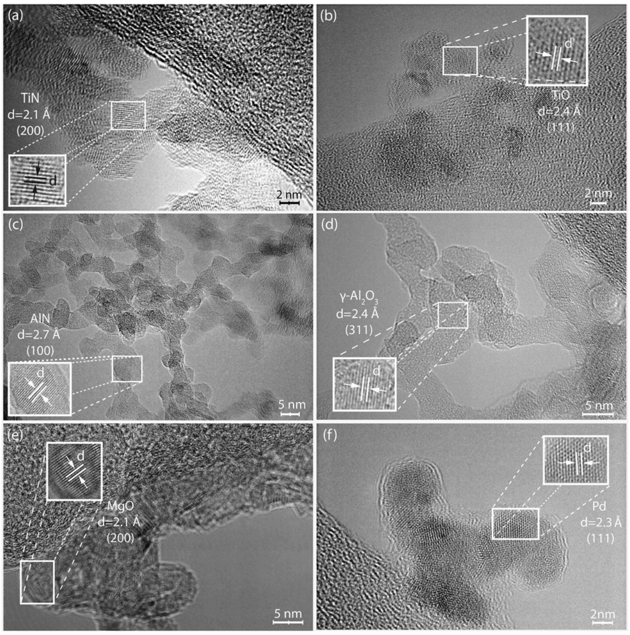

Fig. 2 TEM images of the as-deposited NPs when using (a) and (b) Ti, (c) and (d) Al, (e) Mg and (f) Pd electrodes in the SDG, with N_2 as a carrier gas.

of γ-Al_2O_3 from the peak at 45.7° and found to be 18.4 nm. The crystallite size of MgO was estimated from the peak at 42.9° and determined to be 51.8 nm. Finally, the crystallite size of Pd NPs was estimated from the peak at 40.1° and found to be 54.1 nm.

Fig. 2 shows the TEM images of the as-deposited NPs using Ti, Al, Pd and Mg electrodes in the SDG. All the NPs are agglomerates, comprising of primary particles having sizes that range from *ca.* 5 to 10 nm, corroborating earlier findings.[40] The discrepancy between the primary particle sizes (5–10 nm) observed by TEM and the larger crystallite sizes (*e.g.*, 14.4 nm for AlN) estimated from the XRD using the Scherrer equation suggests that the NPs comprise crystalline domains embedded within partially amorphous phases as reported previously.[44] Alternatively, the difference may also arise from the presence of larger ''splashing particles'' generated by the sparking process, which despite their low number density, can disproportionately influence the XRD peak broadening and thus lead to an overestimation of the average crystallite size (see Fig. S3, SI).[36]

Fig. 2 also show the distance between the atoms (*d*-spacings) of the crystals in the NPs produced by the SDG. The d-spacing measured for TiN is 2.1 Å, corresponding to the (200) plane, and for TiO 2.4 Å, corresponding to the (111) plane; see Fig. 2a and b, respectively. In a similar manner, the d-spacings obtained for the AlN and γ-Al_2O_3 NPs are 2.7 Å (Fig. 2c) and 2.4 Å (Fig. 2d), corresponding to the (100) and (311) planes, respectively. The cases of the NPs produced by the Mg and Pd electrodes are more clear, with the d-spacing of the former being 2.1 Å (corresponding to the (220) plance of MgO; Fig. 1e) and of the latter 2.3 Å (corresponding to the (111) plane; Fig. 1f). For Ti and Al, TEM analysis reveals distinct NP populations consisting of either nitrides or oxides, rather than mixed-phase particles. This demonstrates that the generated aerosol and collected powders are externally mixed, with separate nitride and oxide NPs coexisting in different regions.

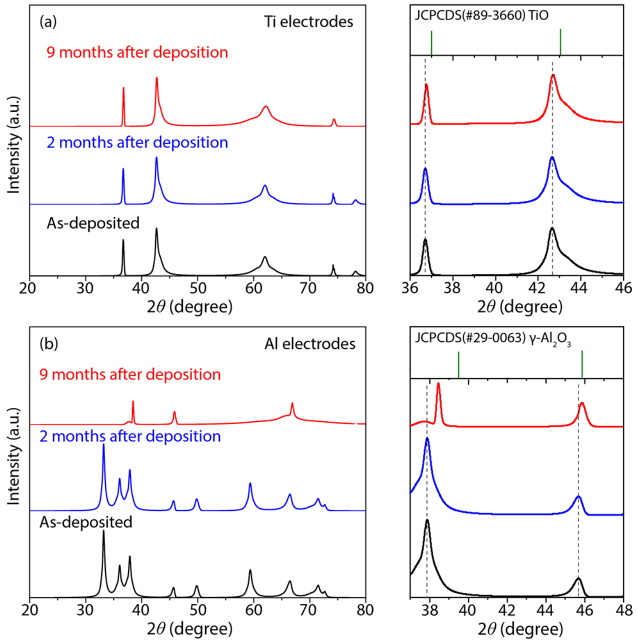

Fig. 3 XRD analysis of NP samples produced by the SDG when using (a) Ti and (b) Al electrodes under N_2 flow. The samples were analyzed immediately after (black curves), two months after (blue curves) and nine months after (red curves) their synthesis. The plots on the right show details of the diffractograms for 2θ = 36–46° for Ti (top) and for 2θ = 37–48° for Al (bottom) electrodes, together with data from libraries corresponding to TiO and γ-Al_2O_3 (green color).

To test whether TiN and AlN undergo oxidation upon exposure to ambient air after synthesis, we conducted XRD measurements of the samples over periods of several months from their synthesis. Fig. 3 shows diffractograms of as-deposited NPs synthesized using Ti or Al electrodes immediately (black color), two months (blue color), and nine months (red color) after production. After two months the diffractograms of the NPs synthesized using Ti and Al electrodes are similar with the as-deposited NPs, indicating that the resulting TiN/TiO and the AlN/γ-Al_2O_3 NP mixtures are stable for two months. After nine months the peaks of TiN slightly shifted to higher 2θ values, indicating the formation of TiN_yO_x.[60] This is corroborated by STEM-EDS mapping of NPs produced using Ti electrodes nine months after synthesis (Fig. 4). In fact, the results of Fig. 4 show higher oxygen content compared to nitrogen, which is in agreement with the XRD results (Fig. 3), suggesting the coexistence of both TiN_yO_x and TiO phase in the system, after nine months from their synthesis. In contrast, the diffractograms of the NPs produced using Al electrodes indicate that the material fully converted to γ-Al_2O_3 after a period of nine months (Fig. 3b).

4. Discussion

Using N_2, with a 99.999% purity, as a carrier gas in atmospheric-pressure spark ablation, can produce mixtures of

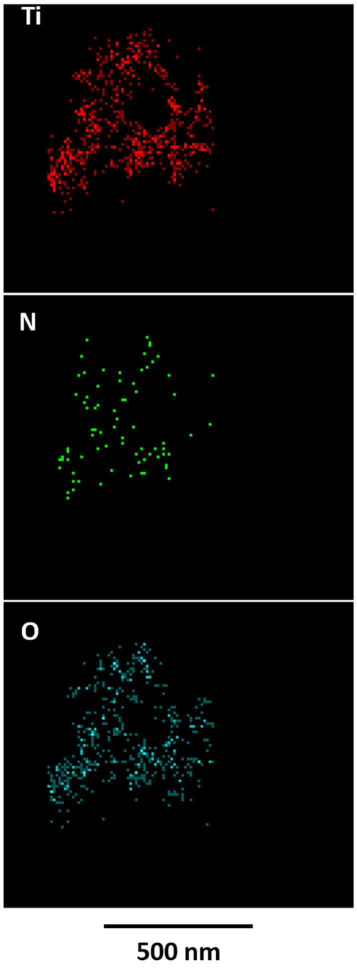

Fig. 4 STEM-EDS mapping of NPs produced by the SDG when using Ti electrodes after nine months from their synthesis.

metal nitride and metal oxide NPs. Metal nitride NPs form by reactive nitrogen species upon braking N_2 in the plasma, which can in turn combine with the metal vapors produced from the ablation of the electrodes. Metal oxide NPs can form in a similar manner because O_2 is present at trace amounts in the carrier gas. Further removing oxygen from the carrier gas, which can be achieved by introducing NPs that can act as O_2 scavengers,[61] can in principle suppress oxide formation and enable the selective synthesis of phase-pure metal nitride NPs. This, however, is out of the scope of the current study, and has not been investigated.

The enthalpies of formation of metal nitrides through the reaction $M + 1/2N_2 \rightarrow MN$, where M is the metal, are negative for Ti, Al and Mg (see Table S1 in the SI), suggesting that TiN, AlN, and Mg_3N_2, can readily form. Among these species, only Ti and Al appear to form mixtures of nitride and oxide NPs as indicated by the XRD measurements provided in the previous section, whereas Mg yields only oxide NPs. In fact, the color of the deposited NPs when ablating Mg electrodes was yellow-green (see Fig. S4 in the SI), but turned white after a few hours, indicating that Mg_3N_2 NPs form initially in the SDG but oxidized rapidly to MgO upon exposure to laboratory air. We should note here that conversion from nitrides to oxides was also observed for the Al-based NPs but that happened much slower, requiring several months. We should note here that the Gibbs free energy for the formation of the different types of NPs would have been a more rigorous thermodynamic descriptor for explaining our results. However, considering that the entropic contributions for the mechanisms under consideration are relatively small compared to the large enthalpy changes (hundreds of kJ mol^{-1}), using the enthalpies for a qualitative explanation of our results is a reasonable and sufficient approximation.

In contrast to Ti, Al, and Mg, the NPs produced by spark ablating Pd electrodes were purely metallic, something that can be explained by the positive enthalpy of formation of PdN_2 (see Table S1 in the SI). In fact, PdN_2 can form under high-pressure conditions ($\sim$58 GPa),[62] but this is typically metastable and eventually breaks down into its more stable metallic form at normal conditions.

The degree to which metal nitride NPs are stabled can be explained by the type of bonding between metal and N atoms, and the associated thermodynamic properties (enthalpy changes for the oxidation of metal nitrides). For instance, the bonds between the Mg and N atoms in Mg_3N_2 are primarily ionic, lacking the stability of covalent or metallic bonding, which yield a weak lattice energy. As a result, it can readily form MgO upon exposure to oxygen or water. AlN, while more stable than Mg_3N_2, primarily exhibits polar covalent bonding between the Al and the N atoms, and lacks d-orbital interaction. This, combined with a highly exothermic oxidation reaction ($2AlN + 1.5O_2 \rightarrow Al_2O_3 + N_2$, $\Delta H = -1035.9$ kJ mol^{-1}), makes AlN thermodynamically prone to oxidation. TiN exhibits mixed bonding, including a significant ionic and covalent component (*e.g.*, Ti–N) arising from its d-p orbital overlap, as well as metallic bonding (*e.g.*, Ti–Ti). These bonds contribute to higher chemical stability, and while oxidation is thermodynamically favorable when exposed to air ($TiN + O_2 \rightarrow TiO_2 + 0.5N_2$, $\Delta H = -656.6$ kJ mol^{-1}), the higher activation energy required for the oxidative cleavage of the Ti–N and Ti–Ti bonds significantly slows oxidation under standard conditions. These interactions contribute to the high lattice stability of TiN and its resistance to oxidation under normal conditions. In contrast, the differences in oxidation behavior among metal nitrides underscores the importance of their stability for high-temperature catalytic applications.

XRD and STEM-EDS analyses (see Fig. 3 and 4) show some oxidation of the TiN NPs after nine months from their synthesis. The oxidation of TiN occurs in three distinct stages:[8] initially, oxygen diffuses into the TiN lattice, replacing nitrogen with oxygen to form titanium oxynitride. This process is limited to the near-surface region and does not involve oxygen penetration deep into the particle core. In the second stage, a natural protective film composed of Ti_nO_{2n-1} phases forms on the surface. This phase transition represents a diffusion-controlled oxidation process, where the oxidation rate is governed by oxygen diffusion through the growing oxide layer. In the final stage, the remaining TiN undergoes slow oxidation as the material becomes progressively coated with a stable TiO_2 layer, further inhibiting oxygen penetration into the core. Nevertheless, TiN is stable for a significantly longer period compared to other materials like AlN, which oxidizes more readily due to its weaker Al–N bonds and higher thermodynamic susceptibility to oxidation. The inherent strength of Ti–N bonds, combined with the gradual and self-limiting nature of its oxidation process, allows TiN to retain its nitride structure under conditions where AlN has already fully oxidized. This is supported by the absence of detectable AlN phases in both XRD and TEM analyses, indicating complete conversion to its oxidized form. This remarkable stability, even in the form of particles a few nanometers in diameter, makes TiN an ideal material for applications requiring long-term resistance to oxidative degradation, particularly in harsh environments and/or over extended periods.

Table S1 (SI) provides the enthalpy changes associated with the formation of metal nitrides for elements that can be spark-ablated under atmospheric-pressure conditions. Generally, elements with a negative enthalpy of formation for nitrides can readily form nitrides *via* spark ablation. The degree to which these particles are stable or not, however, is primarily defined by the strength and nature of the M–N bonds, which is linked to their resistance to oxidation (Table S1, SI) and thus the likelihood of the nitrides transforming into oxides. For example, Mg_3N_2, which features weak ionic bonds, oxidizes rapidly—within a few hours—despite having a relatively low enthalpy change for oxidation (-437.7 kJ mol^{-1}). In contrast, TiN is significantly more stable due to its mixed covalent, ionic and metallic bonding, even though its enthalpy changes for oxidation (-656.6 kJ mol^{-1}) is more negative than that of Mg_3N_2. AlN, which exhibits polar covalent bonding, falls between the cases of Ti and Mg, exhibiting moderate stability despite that its enthalpy change of oxidation is even more negative (-1035.9 kJ mol^{-1}) compared to the other two metals. The apparent mismatch between oxidation enthalpy and observed stability indicates that the character of the bonds among the metal and the nitrogen atoms in the metal nitride NPs plays a more decisive role than thermodynamics. Stronger and more directional bonds, as in TiN, seem to confer greater resistance to oxidation, despite that it exhibits a moderate enthalpy change for oxidation.

Our results provide valuable insights that can help predict whether spark ablating metallic electrodes in N_2 can yield nitride NPs, and if those would be stable enough when exposed to an oxidizing atmosphere. Elements such as Pd, Co, and Ni, which exhibit positive enthalpies of formation for their nitrides, are thermodynamically unlikely to form stable nitrides, and thus tend to produce purely metallic NPs. In contrast, many transition metals—including V, Cr, Mn, Fe, *etc.*—along with metalloids such as B, Si, and Ge, and lanthanoids like La, Ce, and Pr, exhibit negative enthalpies of nitride formation (Table S1, SI), and can therefore form metal nitride NPs upon spark ablation. In all these cases, however, formation of the metal oxides is more favourable than metal oxides, and thus spark-ablating these materials under conditions similar to the ones we used here, is expected to lead to mixtures of metal nitride and metal oxide NPs.

The M–N bonding character of the corresponding metal nitrides, and thus the stability of the resulting NPs, varies among these groups: transition metal nitrides typically feature mixed covalent, ionic, and metallic bonding due to d–p orbital overlaps and metal–metal interactions, which confer high stability and conductivity; metalloid nitrides form predominantly covalent bonding; lanthanoid nitrides mainly exhibit ionic bonding with some covalent character from 5d–2p orbital interactions and generally weaker metallic bonding due to localized 4f electrons. Considering the above, and in line with what we have observed in this work, nitrides with mixed covalent, ionic, and metallic bonding—such as TiN, ZrN, HfN, VN, NbN, TaN, CrN, and MoN—are expected to be rather stable, making them promising candidates for catalysis, sensors, electronics, hard coatings, and other advanced technologies.

Conclusions

We have explored atmospheric-pressure spark ablation in a nitrogen-rich environment as a one-step process for synthesizing mixtures of metal nitride and metal oxide NPs. This approach was applied to different electrode materials, including Ti, Al, Mg and Pd. The resulting particles are agglomerates that have sizes ranging from *ca.* 15 to 400 nm, but consist of primary particles that have a diameter of around 5 nm. Our experiments show that using titanium and aluminium electrodes in the SDG, consistently yields mixtures of metal nitride and oxides NPs; TiN/TiO and AlN/γ-Al_2O_3, respectively, with the former exhibiting higher stability and the latter converting entirely to the oxide phase after a long period of time. In contrast, magnesium forms metal oxide NPs under these conditions, due to the rapid oxidation of initially formed Mg_3N_2 upon exposure to air, whereas palladium yields purely metallic NPs.

Overall, our results indicate that the formation and stability of metal nitride NPs by spark ablation are linked to the thermodynamic properties of the materials, particularly the enthalpy of formation of the corresponding nitrides and the nature of the chemical bonding. Apparently, formation of nitrides by spark ablation competes with formation of oxides that result from trace amounts of O_2 in the system, indicating that further purification can warrant formation of pure nitride phases. Metals with strongly negative nitride formation enthalpies and favourable bonding characteristics (*i.e.*, covalent and ionic or polar covalent bonds with nitrogen) are more likely to form stable nitride NPs. These findings are key for designing efficient NP synthesis recipes for use in advanced materials.

Author contributions

Klito C. Petallidou: validation, investigation, visualization, writing – original draft, conceptualization, methodology, supervision, project administration, Dimitris Gounaris: validation, investigation, writing – review & editing, Pau Ternero: validation, investigation, writing – review & editing. Maria E. Messing: writing – review & editing. Andreas Schmidt-Ott: writing – review & editing. George Biskos: conceptualization, methodology, supervision, writing – review & editing.

Conflicts of interest

There are no conflicts to declare.

Data availability

The data supporting this article have been included as part of the supplementary information (SI). Supplementary information is available. See DOI: https://doi.org/10.1039/d5tc02874d.

Acknowledgements

This work was supported by the Research and Innovation Foundation (Cyprus) under grant EXCELLENCE/0524/0406 (SUNRISE), the European Union's H2020 MSCA (Grant No. 945378, GenerationNano), and the Swedish Research Council (Project No. 2023-05120).

References

1 I. Ashraf, S. Rizwan and M. Iqbal, *Front. Mater.*, 2020, **7**, 181.
2 K. Setoura and S. Ito, *AIP Adv.*, 2021, **11**, 115027.
3 W. Li, U. Guler, N. Kinsey, G. V. Naik, A. Boltasseva, J. Guan, V. M. Shalaev and A. V. Kildishev, *Adv. Mater.*, 2014, **26**, 7959–7965.
4 G. V. Naik, V. M. Shalaev and A. Boltasseva, *Adv. Mater.*, 2013, **25**, 3264–3294.
5 U. Guler, A. Boltasseva and V. M. Shalaev, *Science*, 2014, **344**, 263–264.
6 A. B. Dongil, *Nanomaterials*, 2019, **9**, 1111.
7 S. H. C. Askes, N. J. Schilder, E. Zoethout, A. Polman and E. C. Garnett, *Nanoscale*, 2019, **11**, 20252–20260.
8 B. Avasarala and P. Haldar, *Electrochim. Acta*, 2010, **55**, 9024–9034.
9 X. Li, *Chem. Pap.*, 2024, **78**, 1157–1166.
10 A. Hermawan, Y. Asakura and S. Yin, *Int. J. Miner., Metall. Mater.*, 2020, **27**, 1560–1567.
11 X. Zhao, Z. Xu, Z. Zhang, J. Liu, X. Yan, Y. Zhu, J. P. Attfield and M. Yang, *Nat. Commun.*, 2025, **16**, 182.
12 B. Gao, X. Li, K. Ding, C. Huang, Q. Li, P. K. Chu and K. Huo, *J. Mater. Chem. A*, 2019, **7**, 14–37.
13 M.-S. Balogun, W. Qiu, W. Wang, P. Fang, X. Lu and Y. Tong, *J. Mater. Chem. A*, 2015, **3**, 1364–1387.
14 M. S. Chavali and M. P. Nikolova, *SN Appl. Sci.*, 2019, **1**, 607.
15 W. Xiong, H. Yin, T. Wu and H. Li, *Chem. – Eur. J.*, 2023, **29**, e202202872.
16 A. Al Miad, S. P. Saikat, Md. K. Alam, Md Sahadat Hossain, N. M. Bahadur and S. Ahmed, *Nanoscale Adv.*, 2024, **6**, 4781–4803.
17 C. Wang, L. Yin, L. Zhang, D. Xiang and R. Gao, *Sensors*, 2010, **10**, 2088–2106.
18 N. Goel, K. Kunal, A. Kushwaha and M. Kumar, *Eng. Rep.*, 2023, **5**, e12604.
19 I. Shaheen, I. Hussain, T. Zahra, M. S. Javed, S. S. A. Shah, K. Khan, M. B. Hanif, M. A. Assiri, Z. Said, W. U. Arifeen, B. Akkinepally and K. Zhang, *J. Energy Storage*, 2023, **72**, 108719.
20 C. An, Y. Zhang, H. Guo and Y. Wang, *Nanoscale Adv.*, 2019, **1**, 4644–4658.
21 G. Oskam, *J. Sol-Gel Sci. Technol.*, 2006, **37**, 161–164.
22 U. V. Alpen, A. Rabenau and G. H. Talat, *Appl. Phys. Lett.*, 1977, **30**, 621–623.
23 S. E. Pratsinis, G. Wang, S. Panda, T. Guiton and A. W. Weimer, *J. Mater. Res.*, 1995, **10**, 512–520.
24 S. V. Didziulis, K. D. Butcher and S. S. Perry, *Inorg. Chem.*, 2003, **42**, 7766–7781.
25 A. J. Cinthia, G. S. Priyanga, R. Rajeswarapalanichamy and K. Iyakutti, *J. Phys. Chem. Solids*, 2015, **79**, 23–42.
26 T. Guo, M.-S. Yao, Y.-H. Lin and C.-W. Nan, *CrystEngComm*, 2015, **17**, 3551–3585.
27 W. Luo, F. Shen, C. Bommier, H. Zhu, X. Ji and L. Hu, *Acc. Chem. Res.*, 2016, **49**, 231–240.
28 N. Goel, K. Kunal, A. Kushwaha and M. Kumar, *Eng. Rep.*, 2023, **5**, e12604.
29 I. Shaheen, I. Hussain, T. Zahra, M. S. Javed, S. S. A. Shah, K. Khan, M. B. Hanif, M. A. Assiri, Z. Said, W. U. Arifeen, B. Akkinepally and K. Zhang, *J. Energy Storage*, 2023, **72**, 108719.
30 T. Guo, M.-S. Yao, Y.-H. Lin and C.-W. Nan, *CrystEngComm*, 2015, **17**, 3551–3585.
31 S. Laurent, D. Forge, M. Port, A. Roch, C. Robic, L. Vander Elst and R. N. Muller, *Chem. Rev.*, 2008, **108**, 2064–2110.
32 W. Tillmann, D. Kokalj, D. Stangier, Q. Fu and E. Kruis, *Thin Solid Films*, 2019, **689**, 137528.
33 D. Kiesler, T. Bastuck, R. Theissmann and F. E. Kruis, *J. Nanopart. Res.*, 2015, **17**, 152.
34 M. Quast, P. Mayr and H.-R. Stock, *Surf. Coat. Technol.*, 1999, **120–121**, 244–249.
35 H. R. Stock, C. Jarms, F. Seidel and J. E. Döring, *Surf. Coat. Technol.*, 1997, **94–95**, 247–254.
36 *Spark ablation: building blocks for nanotechnology*, ed. A. Schmidt-Ott, Jenny Stanford Publishing, Singapore, 2020.
37 G. Biskos, V. Vons, C. U. Yurteri and A. Schmidt-Ott, *KONA*, 2008, **26**, 13–35.
38 C. Loizidis, K. C. Petallidou, A. Maisser, S. Bezantakos, T. V. Pfeiffer, A. Schmidt-Ott and G. Biskos, *Aerosol Sci. Technol.*, 2024, **58**, 1421–1431.
39 A. Maisser, K. Barmpounis, M. B. Attoui, G. Biskos and A. Schmidt-Ott, *Aerosol Sci. Technol.*, 2015, **49**, 886–894.
40 J. Feng, G. Biskos and A. Schmidt-Ott, *Sci. Rep.*, 2015, **5**, 15788.

41 B. O. Meuller, M. E. Messing, D. L. J. Engberg, A. M. Jansson, L. I. M. Johansson, S. M. Norlén, N. Tureson and K. Deppert, *Aerosol Sci. Technol.*, 2012, **46**, 1256–1270.

42 T. V. Pfeiffer, J. Feng and A. Schmidt-Ott, *Adv. Powder Technol.*, 2014, **25**, 56–70.

43 M. E. Messing, R. Westerström, B. O. Meuller, S. Blomberg, J. Gustafson, J. N. Andersen, E. Lundgren, R. Van Rijn, O. Balmes, H. Bluhm and K. Deppert, *J. Phys. Chem. C*, 2010, **114**, 9257–9263.

44 K. C. Petallidou, P. Ternero, M. E. Messing, A. Schmidt-Ott and G. Biskos, *Nanoscale Adv.*, 2023, DOI: 10.1039/D3NA00152K.

45 M. Snellman, N. Eom, M. Ek, M. E. Messing and K. Deppert, *Nanoscale Adv.*, 2021, **3**, 3041–3052.

46 N. S. Tabrizi, Q. Xu, N. M. van der Pers and A. Schmidt-Ott, *J. Nanopart. Res.*, 2010, **12**, 247–259.

47 K. C. Petallidou, A. Schmidt-Ott and G. Biskos, *Aerosol Sci. Technol.*, 2024, **58**, 1079–1088.

48 C. Roth, G. A. Ferron, E. Karg, B. Lentner, G. Schumann, S. Takenaka and J. Heyder, *Aerosol Sci. Technol.*, 2004, **38**, 228–235.

49 S. Ghaemi, A. Schmidt-Ott and F. Scarano, *Meas. Sci. Technol.*, 2010, **21**, 105403.

50 C. Roth, G. A. Ferron, E. Karg, B. Lentner, G. Schumann, S. Takenaka and J. Heyder, *Aerosol Sci. Technol.*, 2004, **38**, 228–235.

51 V. A. Vons, A. Anastasopol, W. J. Legerstee, F. M. Mulder, S. W. H. Eijt and A. Schmidt-Ott, *Acta Mater.*, 2011, **59**, 3070–3080.

52 J. Elmroth Nordlander, M. Bermeo, P. Ternero, D. Wahlqvist, T. Schmeida, S. Blomberg, M. E. Messing, M. Ek and J.-M. Hübner, *Materials*, 2023, **16**, 1113.

53 F. Radovanović-Perić, M. Burtscher, I. Panžić, D. Kiener and V. Mandić, *Ceram. Int.*, 2024, S0272884224034436.

54 M. A. Signore, A. Della Torre, A. Serra, D. Manno, R. Rinaldi, M. Mazzeo, L. N. Francioso and L. Velardi, *Crystals*, 2025, **15**, 587.

55 P. Scherrer, *J. Nachr. Ges. Wiss. Göttingen*, 1918, **26**, 98–100.

56 C. A. Schneider, W. S. Rasband and K. W. Eliceiri, *Nat. Methods*, 2012, **9**, 671–675.

57 F. Radovanović-Perić, M. Burtscher, I. Panžić, D. Kiener and V. Mandić, *Ceram. Int.*, 2025, **51**, 5576–5582.

58 V. Fournier, P. Marcus and I. Olefjord, *Surf. Interface Anal.*, 2002, **34**, 494–497.

59 A. L. Patterson, *Phys. Rev.*, 1939, **56**, 978–982.

60 W. Chen, J. Li, Z. Wang, H. Wang, Y. Li and L. Tang, *Dalton Trans.*, 2024, **53**, 1265–1273.

61 V. Olszok, M. Bierwirth and A. P. Weber, *ACS Appl. Nano Mater.*, 2023, **6**, 1660–1666.

62 D. Åberg, P. Erhart, J. Crowhurst, J. M. Zaug, A. F. Goncharov and B. Sadigh, *Phys. Rev. B*, 2010, **82**, 104116.